Proceedings of 2005 CACS Automatic Control Conference
Tainan, Taiwan, Nov 18-19, 2005

Dual-Stage Piezoelectric Nano-Positioner Utilizing an Optical Fiber Fabry-Perot Interferometer

Shao-Kang Hung and Li-Chen Fu
Department of Electrical Engineering, National Taiwan University
No.1, Sec. 4, Roosevelt Rd., Taipei, Taiwan 106, (skhung, lichen)@ntu.edu.tw

Abstract

This paper proposes a new modulation scheme using high order harmonic information to solve the so-called ambiguity problem of interferometry. To start with, we build a Fiber Fabry-Perot Interferometer to serve as a displacement sensor, which has two operation modes, coarse and fine modes. Integrating the afore-developed sensor, a piezoelectric actuator, and a scheduled proportional-integral/adaptive-sliding controller, we construct a dual-stage nano-positioning system. The experimental results show that the proposed system has the capability to extend the positioning range beyond the limit of the wavelength while keeping the naturally high resolution, ±5nm, of interferometry.

Key Word: adaptive-sliding control, interferometer, optical fiber, nano-positioning, modulation.

1. Introduction

Interferometry has excellent sensitivity [1] and is used in various measurements, such as temperature [2], strain [3], magnetic field [4], angular velocity [5], and many other physical parameters [6]. The largest advantage of optical interferometry is also its main disadvantage. Due to the short wavelength of the light, the sensitivity of a single wavelength interferometer is very high, but also due to the short wavelength the dynamic range is limited unless additional information is available. To extend the measurement range, four classifications of methods were proposed: white-light interferometry [7], dual-wavelength inteferometry [8, 9], phase-shifting interferometry [3], and modulation techniques [10, 11]. If a white light source is used in an interferometer the best contrast interference fringes obtained only when the two paths in the interferometer are equal. Dual-wavelength method is to perform the measurement at two wavelengths and compare the measurement data for the different wavelengths to determine the true optical path difference (OPD).

The optical phase is a function of the wavelength and OPD. Thus modulation can be implemented on these two variables by oscillating them at a relatively high frequency. It is difficult to change the wavelength of a laser device without changing its intensity [11]. More complicated optical and electrical equipments are needed to compensate the unstable intensity of the laser source. This paper chooses the displacement modulation method to break the ambiguity. Utilizing high order harmonic information, solidly digital signal can be obtained to achieve far-reaching measurement with coarse resolution $\lambda/8$. Combining with the naturally fine resolution of interferometry, a powerful displacement sensor having both long measurement range and high resolution was developed. We designed, analyzed and built a Fiber Fabry-Perot Interferometer (FFPI). Utilizing this powerful sensor, we develop a positioner according to the sensor's dual-mode nature.

2. FFPI Sensing System

2-1 Working Principle of FFPI

Fabry-Perot interferometer makes use of multiple reflections between two closely spaced partially reflective interfaces. Part of the light is transmitted each time the light reaches the second surface, resulting in multiple beams which can interfere with each other. The large number of interfering rays produces an interferometer with extremely high resolution, somewhat like the multiple slits of a diffraction grating increase its resolution.

If the polished optical fiber end is used to be the interface of the Fabry-Perot cavity, this kind of device is called FFPI. Figure 1 illustrates the configuration of FFPI. The laser diode emits the light into 1st arm of the Y-shaped fiber coupler. After the optical interference occurred at the fiber end of 2nd arm, the interfered fringe signal can be received by a photo-detector installed at the end of 3rd arm.

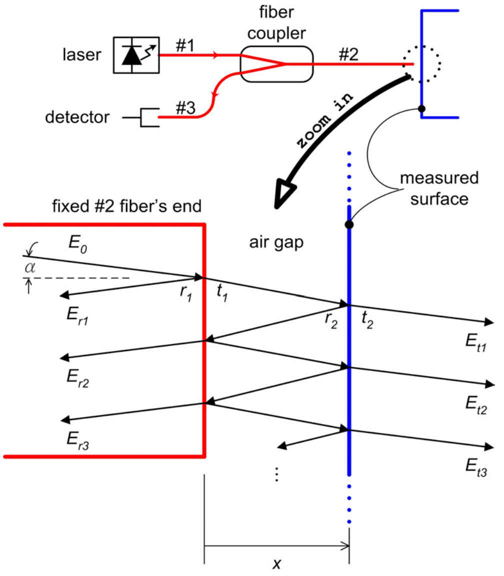

Figure 1. The configuration of the Fiber Fabry-Perot Interferometer.

As the normally incident light reaches the fiber end of 2nd arm, part of it is reflected back by the interface between fiber and the air while the other part transmits. Zero absorption is assumed. The partial reflection/transmission behavior will happen for infinite times. Optical interference can occur in both groups of light. Starting with the intensity of the incident light I_0, its corresponding electric field is denoted as $E_0 e^{\omega t}$. The k^{th} reflected electric field from the first interface is denoted as E_{rk}, while the k^{th} partially transmitted electric field through the second interface is denoted as E_{tk}. The coefficients of amplitude reflection, r_1, and transmission, t_1, denote light traveling through the first interface while the coefficients, r_2 and t_2, denote light traveling through second interface. The multiple output beams differ in phase due to the different path lengths traversed by each of the beams. The optical phase acquired by the light on one round trip through the cavity is given by:

$$\phi = \frac{4\pi n x \cos\alpha}{\lambda}, \tag{1}$$

where λ = the wavelength of the laser
α = the incident angle
n = the refraction index of the cavity
x = the gap distance between two interfaces.

Since $n = 1$ for air and perpendicular incidence, Eq. (1) can be simplified into

$$\phi = \frac{4\pi x}{\lambda}. \tag{2}$$

The electric field of each of the transmitted waves can thus be written as:

$$\begin{aligned}
E_{t1} &= (E_0 e^{\omega t})(t_1 i)(t_2 i) \\
E_{t2} &= (E_0 e^{\omega t})(t_1 i)(-r_2)(-r_1)(t_2 i)\cdot e^{i\phi} \\
E_{t3} &= (E_0 e^{\omega t})(t_1 i)(-r_2)(-r_1)(-r_2)(-r_1)(t_2 i)\cdot e^{i2\phi} \\
&\vdots \\
E_{tk} &= (E_0 e^{\omega t}) t_1 t_2 (r_1 r_2 e^{i\phi})^{k-1}, \quad k \in N.
\end{aligned} \tag{3}$$

The electric field of the interfered waves, E_t, is

$$E_t = \sum_{k=1}^{\infty} E_{tk} = (E_0 e^{\omega t}) \cdot \frac{-t_1 t_2}{1 - r_1 r_2 \cdot e^{i\phi}}. \tag{4}$$

If the two interfaces are the same, we have $t_1 = t_2 \equiv t$ and $r_1 = r_2 \equiv r$. Introducing the power reflectivity $R = r^2$ with lossless assumption $r^2 + t^2 = 1$, we can find the normalized power transmission as:

$$\frac{I_t}{I_0} = \left|\frac{E_t}{E_0}\right|^2 = \frac{(1-R)^2}{1 + R^2 - 2R\cos\phi}, \tag{5}$$

which is known as Airy Function [12]. On the other hand, the electric field of the reflected group can be expressed as:

$$\begin{aligned}
E_{r1} &= (E_0 e^{\omega t})(-r_1) \\
E_{r2} &= (E_0 e^{\omega t})(t_1 i)(-r_2)(t_1 i)\cdot e^{i\phi} \\
E_{r3} &= (E_0 e^{\omega t})(t_1 i)(-r_2)(-r_1)(-r_2)(t_1 i)\cdot e^{i2\phi} \\
&\vdots \\
E_{rk} &= (E_0 e^{\omega t}) \frac{t_1^2}{r_1} (r_1 r_2 e^{i\phi})^{k-1}, \quad k \in N - \{1\}.
\end{aligned} \tag{6}$$

If the two interfaces are the same, i.e. $r_1 = r_2$, all of E_{rk} form a geometric sequence. The normalized power reflection can easily be found as [13]:

$$\frac{I_t}{I_0} = \left|\frac{\sum_{k=1}^{\infty} E_{rk}}{E_0}\right|^2 = \frac{2R(1-\cos\phi)}{1 + R^2 - 2R\cos\phi}. \tag{7}$$

However if the material of the measured surface is different from the sensing fiber, the geometric relation vanishes. The normalized power reflection should be derived into a more complicated form:

$$\frac{I_t}{I_0} = \left|\frac{\sum_{k=1}^{\infty} E_{rk}}{E_0}\right|^2 = \frac{R_1 + R_2 - 2\sqrt{R_1 R_2}\cos\phi}{1 + R_1 R_2 - 2\sqrt{R_1 R_2}\cos\phi}, \tag{8}$$

where R_1 and R_2 are the power reflectivity of the first and the second interfaces , respectively. R_1 is 3.5% for the interface between glass and air. When the gap distance $x = 0$, R_2 is 0.9 for the interface between air and the measured object, a golden coated mirror. As the gap distance increases the power coupled back to the fiber decreases [14]. The equivalent reflectivity is

$$R_2 = 0.9 \cdot \left\{\frac{a}{a + 2x\tan[\sin^{-1}(NA)]}\right\}^2, \tag{9}$$

where a and NA are the fiber core radius and the numerical aperture, respectively. The transduced signal can be represented by Eq. (8). Substituting the parameters of $a = 4.15\ \mu m$, $NA = 0.13$ and $\lambda = 1.31\ \mu m$, we have the simulation result in Fig. 2. Further modulator design bases on this mathematical model.

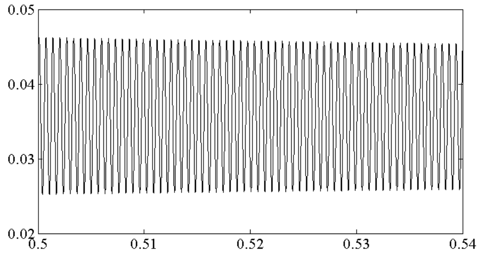

Figure 2. The plot of I_r/I_0 vs gap distance x.

2-2 Modulation and Demodulation

In Fig. 2, the signal oscillates by the period of $\lambda/2$. Local maximum represents constructive interference while local minimum means destructive interference. As the gap distance x increases the amplitude decreases. In fact, the DC value also slightly changes with x. The received signal can be approximated to:

$$I_r = A(x)\cdot\left[-\cos(\frac{4\pi x}{\lambda})\right]+D(x), \qquad (10)$$

where A(x) and D(x) represent the variant amplitude and DC value, respectively. Thus it is difficult to reveal x from the ambiguous fringe signal directly. In order to get rid of this predicament, we design two terms:

$$\begin{cases} g \equiv sign(\dfrac{dI_r}{dx}) \\ h \equiv sign(\dfrac{d^2I_r}{dx^2}) \end{cases} \qquad (11)$$

In order to obtain g and h signals, the phase-sensitive detection technique is adopted [15]. A relative high frequency sinusoidal signal is applied on a small piezoelectric stack to oscillate the fiber end slightly. This modulating action will induce certain response on the signal I_r at the identical frequency. The lock-in amplifier (SR830, Stanford Research Systems Inc.) can resolve such little response and give an output phase signal. If the response and the modulation signal are in-phase or out-of-phase, the output phase signal is positive or negative, respectively. Obviously this output phase signal is the previously defined g-signal. The lock-in amplifier can also give the 2nd harmonic phase signal. That is the source the h-signal can be obtained.

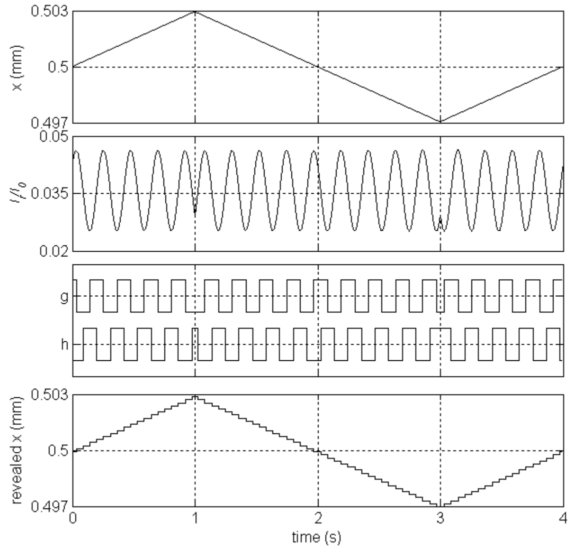

Figure 3. The functionality of g-signal and h-signal.
As x changes its direction, the lead-lag relation between g-signal and h-signal changes correspondingly.

The following simulation demonstrates the functionality of these two terms in Eq. (11). In Fig. 3., as x increases g-signal lags h-signal by 90°. On the contrary, g-signal leads h-signal by 90° when x moves to the opposite direction. This coding characteristic is the same with "incremental encoders", which are widely used to measure angular or linear position. Both g and h signals are fed into an accurate direction-detecting circuit [16]. Counting the output up/down clocks, we can reveal x with the resolution of $\lambda/8$, 163.75nm. It is labeled as "coarse mode". Since the direction-detecting circuit and the counter only consist of logic components, the response speed can be fast. Naturally fine resolution of interferometry is not used so far. Now we turn to deal with the original signal of I_r. Using "coarse mode" to pre-scan a wide range of x, we can find enough accurate $A(x)$ and $D(x)$ since they don't have great gradient values. A new signal can be defined as:

$$f \equiv \left[-\cos(\frac{4\pi x}{\lambda})\right] = \frac{[I_r - D(x)]}{A(x)} \in [-1, 1] \qquad (12)$$

Bundled (g, h) signal also gives the quadrant information of f-signal. It can be observed in Fig. 3. that (+,+) indicates the 1st quadrant, (+,-) indicates the 2nd, etc. Knowing exact quadrant information, high resolution x can be revealed from the f-signal utilizing inverse-trigonometry [3]. In order to pursue extreme resolution, a low-pass filter is adopted to suppress the noise on f-signal. Further experiment shows that the resolution of such "fine mode" can reach ±5nm. Hence, a displacement sensor having both long measurement range and high resolution is developed by fusion of "coarse mode" and "fine mode".

3. Controller Design

We design two individual controllers for coarse mode and fine mode, since their characteristics are much different. Fine mode has higher resolution but slower response than coarse mode. A classical proportional-integral (PI) controller is chosen for coarse mode while an adaptive sliding-mode controller is designed for fine mode. Rate limiters are attached at the outputs of the controllers in order not to drive the actuator beyond the maximum sensing speed of the FFPI. A superior scheduler is also designed to switch the operation between coarse mode and fine mode.

3-1 Adaptive Sliding-Mode Controller

In order to design a controller which possesses a good capability to deal with the piezoelectric nonlinearity, the uncertainty, meanwhile the high robustness, and the self-tuning property, we propose an adaptive sliding-mode controller for FFPI's "fine mode" operation. To start with, a linear second order model can be used to represent the actuator's nominal dynamics:

$$\ddot{x} + a_1\dot{x} + a_0 x = bu\,, \tag{13}$$

where x stands for the displacement of the actuator, b is the forcing coefficient of the control input u, a_1 and a_0 represent the damping and the stiffness of the system, respectively. The parameters a_1, a_0 and b can be well estimated via an off-line identification test.

Then, then system dynamics can be transformed into error coordinates using the relation $e = x - x_d$, where x_d represents the desired trajectory. Use the compact notations, $A = [-a_1 \ \ -a_0]$; $X = [\dot{x} \quad x]^T$, we have

$$\ddot{e} = AX + bu - x_d\,. \tag{14}$$

Nevertheless, we add an additional term to represent the noise, the disturbance and the actuator's piezoelectric hysteresis behavior as:

$$\ddot{e} = AX + bu - x_d + w\,, \tag{15}$$

where w is assumed bounded. Then, we divide this term into two parts, one is a constant uncertainty w_c and the other one is a varying uncertainty w_v, which is assumed bounded and satisfies $|w_v| \le w_{max}$. Therefore, Eq. (15) can be expressed as:

$$\ddot{e} = AX + bu - x_d + w_c + w_v\,. \tag{16}$$

A first order sliding surface, s, is chosen such that:

$$s = \dot{e} + \gamma e\,, \tag{17}$$

where γ is a positive scalar to be designed. The sliding surface is designed such that the system is stable when the system state lies on this surface. Therefore, the problem is reduced to guarantee that the state reaches the sliding surface, or in the case of bounded tracking, some region on the surface. Our main purpose is to force the tracking error to zero. Given the initial condition, $x_d(0)=x(0)$, with the initial desired state $x_d(0)$, the tracking problem, $x(t)\to x_d(t)$ as $t\to\infty$, is equivalent to that of remaining on the surface s for all $t > 0$; indeed $s \equiv 0$ represents a linear differential equation whose unique solution is $E \equiv 0$. Then, the sliding surface dynamics can be determined by taking the time derivative of Eq. (17), i.e.,

$$\dot{s} = \ddot{e} + \gamma\dot{e}\,. \tag{18}$$

Then substituting Eq. (16) and (17) into Eq. (18), we have

$$\dot{s} = AX + bu - \ddot{x}_d + \gamma\dot{e} + w_c + w_v\,. \tag{19}$$

Based on Eq. (19), the control law is designed as:

$$u_{AS} = \hat{b}^{-1}(-AX + \ddot{x}_d - \gamma\dot{e} - \hat{w}_c - \kappa s - \eta sat(s))\,, \tag{20}$$

where $\kappa > 0$ and $\eta > |w_{max}|$. Moreover, $\hat{b}$ and $\hat{w}_c$ are the estimated values of b and w_c, respectively, and *sat(.)* is the saturation function defined as:

$$sat(s) \equiv \begin{cases} 1 & \\ \dfrac{s}{|\varepsilon|} & if \quad \begin{matrix} \varepsilon < s \\ -\varepsilon \le s \le \varepsilon \\ s < -\varepsilon \end{matrix}, \\ -1 & \end{cases} \tag{21}$$

Substituting Eq. (20) into Eq. (15), we can obtain

$$\begin{aligned} \ddot{e} &= AX + b\{\hat{b}^{-1}[-AX + x_d - \gamma\dot{e} - \hat{w}_c - \kappa s - \eta sat(s)]\} \\ &\quad - \ddot{x}_d + w_c + w_v \\ &= AX + (\tilde{b} + \hat{b})\{\hat{b}^{-1}[-AX + x_d - \gamma\dot{e} - \hat{w}_c - \kappa s - \eta sat(s)]\} \\ &\quad - \ddot{x}_d + w_c + w_v \\ &= \tilde{b}u_{AS} - \gamma\dot{e} - \kappa s - \eta sat(s) + \tilde{w}_c + w_v \end{aligned} \tag{22}$$

where the estimation error are defined as $\tilde{b} = b - \hat{b}$, and $\tilde{w}_c = w_c - \hat{w}_c$. By applying appropriate gains κ, η, and γ, we can accelerate the convergence and force the error to zero in a shorter period of time. In summary, the proposed adaptive sliding-mode controller is formulated and its stability can be further proven.

3-2 Scheduling Controller

As afore mentioned, a low-pass filter is used in "fine mode" to achieve high resolution, but it also slow down the measurement speed of "fine mode". If we face a high resolution (±5nm) tracking task, there is no reason to use "coarse mode". However, for a regulation task, which requires its transient response to be fast but not necessary to be accurate, the use of "coarse mode" is thus motivated. In this section, we design a superior scheduler to deal with regulation tasks. If the error is greater than 163.75nm, the output of FFPI's "coarse mode," x_{cm}, is fed to the associated PI controller and the scheduler assigns u to u_{PI}. In the other case, the error is less than or equal to 163.75nm, "fine mode" and its associated adaptive-sliding controller are activated. The behavior of the scheduler is expressed in Eq. (23) and fig. 4.

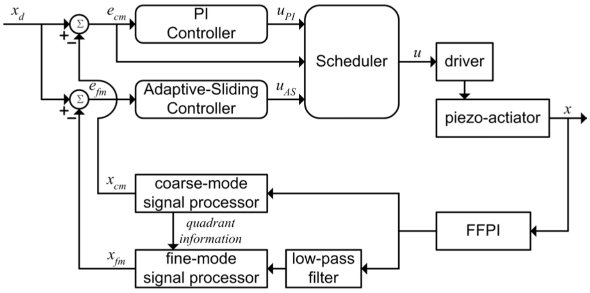

Figure 4. Block diagram of the control loop.

$$u=\begin{cases} u_{PI} & \text{if} \quad e_{cm}>163.75nm \\ u_{AS} & \quad\quad e_{cm}\leq 163.75nm \end{cases}, \tag{23}$$

where

$$\begin{cases} u_{PI}=K_P e_{cm}+K_I\int e_{cm}dt \\ u_{AS}=\hat{b}^{-1}(-AX_{fm}+\ddot{x}_d-\gamma\dot{e}_{fm}-\hat{w}_c-\kappa s_{fm}-\eta sat(s_{fm})) \end{cases}.$$

4. Experiments

4-1 FFPI Test

The experimental setup is illustrated in Fig. 5. The measurand is a mirror with both coated sides. One side is detected by a displacement sensor (laser-based triangulation measurement system MICROTRAK^{TM} 7000, MTI Instruments Inc.) while the other side is detected by our FFPI system. As the piezoelectric actuator carries the mirror to move left-and-right we can compare the results from these two sensors.

The function generator drives the piezoelectric oscillator to have a peak-to-peak 10 nm sinusoidal motion at 10 kHz. The optical fiber end, as the sensing head of our FFPI system, is attached on the piezoelectric oscillator for the purpose of displacement modulation. The laser diode emits 1310 nm wavelength light into the optical fiber coupler. The photo-detector transforms the optical signal into the electrical signal, which represents the interference. The two inputs of the lock-in amplifier #1 are the interference signal, I_r, and the reference signal from the signal generator. The output of the lock-in amplifier #1 is the relative phase difference between the two inputs. The lock-in amplifier #2 provides the 2nd harmonic phase information. After appropriate amplifying and conditioning, the data acquisition card (PCI-DAS1602/16, Measurement Computing Inc.) collects four signals into the computer system. The photograph of proposed system is shown in Fig. 6.

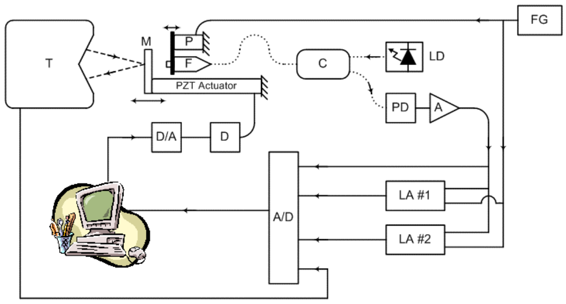

Figure 5. Block diagram of the proposed FFPI system.
Solid lines represent electrical routing. Dashed lines represent the laser path of T. Dotted lines represent the optical fibers.

T: Triangular displacement sensor.
M: Mirror with two coated sides.
P: Piezoelectric oscillator.
F: Fiber connector.
C: Fiber coupler.
LD: Laser diode.
PD: Photo detector.
FG: Function generator.
A: Amplifier.
LA: Lock-in amplifier.
D: Piezo driver.
A/D: A to D converter.
D/A: D to A converter.

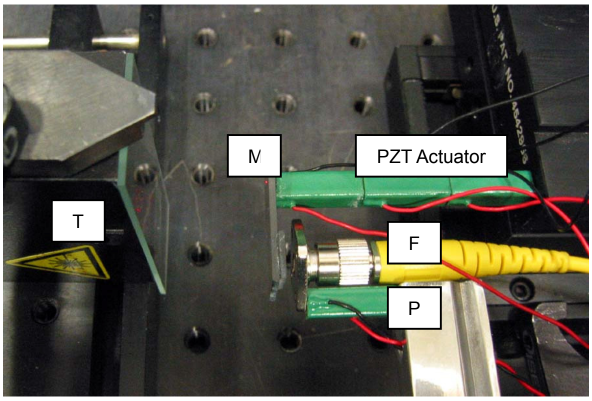

Fig.6. Photograph of the experimental equipments. The labels accord with figure 5.

A series of decaying triangular waves are used to drive the piezoelectric actuator. The hysteresis behavior can be measured by both sensing systems. The result from our FFPI is show in Fig. 7a and Fig. 7b shows the data from the commercial sensor. The correctness of the proposed FFPI system can be assured since the results match with each other.

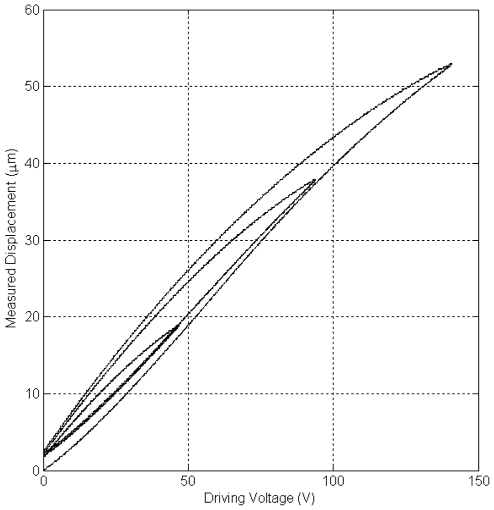

Fig. 7a. Hysteresis measured by the proposed FFPI system.

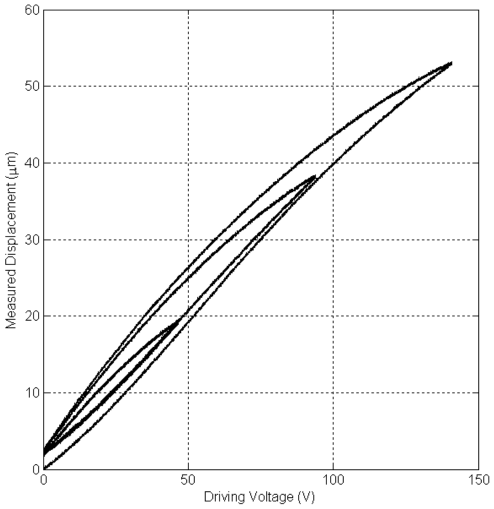

Fig. 7b. Hysteresis measured by a commercial displacement sensor, MICROTRAK^{TM} 7000, MTI Instruments Inc.

4-2 Positioner Test

After testing the functionality of the sensor, the performance of the whole positioner system is tested in this section. Referring to the experimental results in fig. 8, a series of regulation tasks are carried out with the stepping size of 5μm. The enlarged figure is also shown to see the details. From 50ms to 56ms, "coarse mode" and its associated PI controller are selected by the scheduler because the error is still greater than the resolution of "coarse mode," 163.75nm. Therefore, the readout in this stage is quantized by this value. From 56ms to 100ms, the scheduler activates the adaptive sliding controller, which uses the information from "fine mode" processor. The readout in this stage is much finer than coarse mode. After a little chattering during 56ms to 60ms, the steady state resolution can be observed as ±5nm. Regarding to other time domain characteristics in this case, the overshoot is 0.5%, the rise time is 6ms, and the ±0.1% settling time is 10ms.

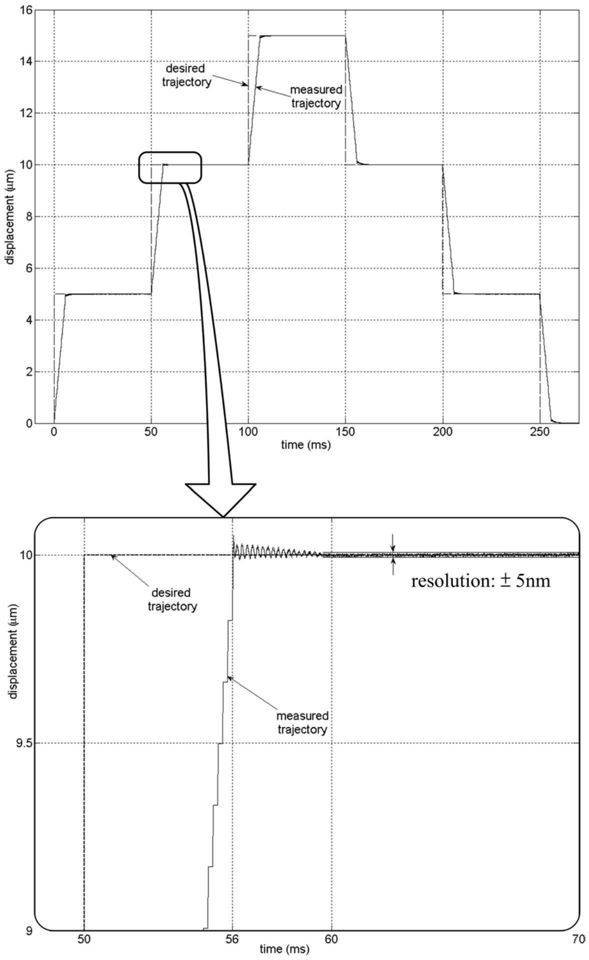

Fig. 8. Step response of the proposed positioning system.

Table 1. Specifications of the proposed FFPI

measurement characteristic	coarse mode	fine mode	scheduling mode
range	**1mm**	163.75nm	**1mm**
resolution	163.75nm	**±5nm**	**±5nm**
speed	1mm/s	20μm/s	20μm/s

5. Conclusion

In this paper, we designed a novel modulation/ demodulation scheme to extend the measurement range beyond the limit of the wavelength of inteferometry successfully. Referring to table 1, the hereby constructed FFPI can operate in coarse and fine modes, which have very different characteristics. The coarse mode's resolution is not very high but it has faster response and longer measurement range than the fine mode. Therefore, we design a fast PI controller for coarse mode and an accurate adaptive sliding controller for fine mode. Furthermore, a scheduler is designed to integrate these two modes so that the overall system has both a long positioning range (full stroke of the actuator, 70μm) and a high resolution, ±5nm.

Theoretically the measurement range should only be limited by the coherence of the laser source. Using the widely used semiconductor laser, the measurement range of our system is examined to reach 1mm. On the other hand, better resolution should be expected if even shorter wavelength is adopted.

6. References

[1] T. Wang, S. Zheng, and Z. Yang, "A High Precision Displacement Densor Using a Low-Finesse Fiber-Optic Fabry-Perot Interferometer," *Sensors and Actuators A.,* vol. 69, 1998, pp. 134-138.

[2] G. B. Hocker, "Fiber-Optic Sensing of Pressure and Temperature," *Appl.Opt.,* vol. 18, no. 9, 1976, pp. 1445-1448.

[3] K. A. Murphy, M. F. Gunther, A. M. Vengsarkar and R. O. Claus, "Quadrature Phase-Shifted, Extrinsic Fabry-Perot Optical Fiber Sensors," *Opt. Lett.,* vol. 16, no. 4, pp. 273-275.

[4] A. Dandridge, A. B. Treven, G. H. Sigel, Jr., E. J. West, and T. G. Giallorenzi, "Optical Fiber Magnetic Field Sensors," *Electron.Lett..,* vol. 16, no. 11, 1980, pp. 408-409.

[5] A. Vali and R. W. Shorthill, "Fiber Ring Interferometer," *Appl. Opt.,* vol. 15, no. 5, 1979, pp. 1445-1448.

[6] T. Yoshino, K. Kurosawa, K. Itoh and T. Ose, "Fiber-Optic Fabry-Perot Interferometer and Its Sensor Applications," *IEEE Trans. Microwave Theory and Techniques,* vol. 30, no. 10, 1982, pp. 1612-1621.

[7] U. Schnell, R. Dandliker, and S. Gray, "Dispersive White-Light Interferometry for Absolute Distance Measurement with Dielectric Multilayer Systems on the Target," *Opt. Lett.,* vol. 21, no. 7, 1996, pp. 528-530.

[8] Y. Y. Cheng and J. C. Wyant, "Multiple-Wavelength Phase-Shifting Interferometry," *Appl. Opt.,* vol. 24, no. 6, 1985, pp. 804-807.

[9] P. J. Groot, "Extending the Unambiguous Range of Two-color Interferometers," *Appl.Opt.,*vol. 33, no. 25, 1994, pp. 5948-5953.

[10] P.-Y. Chien, Y.-S. Chang and M.-W. Chang, "Electrically Nulled Interferometric Sensor Based on Triangular Phase Modulation," *Opt. Commu.,* vol. 135, 1997, pp. 198-202.

[11] S. A. Meller, "Extrinsic Fabry-Perot Interferometer System Using Wavelength Modulated Source," *Master thesis,* 1996.

[12] W. B. Cook, H. E. Snell, and P. B. Hays, "Multiplex Fabry–Perot interferometer:I. Theory," *Appl.Opt.* vol. 34, no. 24, 1995, pp. 5263-5267.

[13] J. L. Santos, A. P. Leite, and D. A. Jackson "Optical Fiber Sensing with a Low-Finesse Fabry-Perot Cavity," *Appl. Opt.,* vol. 31, no. 34, 1992, pp. 7361-7366.

[14] G. Keiser, *Optical Fiber Communications* 2^{nd} *Edition,* McGRAW-Hill Inc., 1991, p. 114.

[15] *Manual of Model SR830 DSP Lock-in Amplifier,* SRS Inc., 2002, pp. 3-1~3-2.

[16] D. W. Pessen, *Industrial Automation,* John Wiley & Sons Inc., 1989, p. 327.